Title

Growth and Photoelectrochemical Energy Conversion of Wurtzite Indium Phosphide Nanowire Arrays

Journal

ACS Nano, 10(5)

ISSN

1936-0851

Authors

Kornienko, Nikolay

Gibson, Natalie A

Zhang, Hao

et al.

Publication Date

2016-05-24

DOI

10.1021/acsnano.6b02083

Peer reviewed

ACSNANO

www.acsnano.org

ARTICLE

Growth and Photoelectrochemical Energy Conversion of Wurtzite Indium Phosphide Nanowire Arrays

Nikolay Kornienko,[†] Natalie A. Gibson,[†,∥] Hao Zhang,[†] Samuel W. Eaton,[†] Yi Yu,[†] Shaul Aloni,[‡] Stephen R. Leone,[†,§,∥] and Peidong Yang*[,†,⊥,∇,○]

[†]Department of Chemistry, University of California, Berkeley, California 94720, United States
[‡]Molecular Foundry, Lawrence Berkeley National Lab, Berkeley, California 94720, United States
[§]Department of Physics, University of California, Berkeley, California 94720, United States
[∥]Chemical Sciences Division, Lawrence Berkeley National Lab, Berkeley, California 94720, United States
[⊥]Department of Materials Science and Engineering, University of California, Berkeley, California 94720, United States
[∇]Materials Sciences Division, Lawrence Berkeley National Lab, Berkeley, California 94720, United States
[○]Kavli Nanoscience Institute, Berkeley, California 94720, United States

Supporting Information

ABSTRACT: **Photoelectrochemical (PEC) water splitting into hydrogen and oxygen is a promising strategy to absorb solar energy and directly convert it into a dense storage medium in the form of chemical bonds. The continual development and improvement of individual components of PEC systems is critical toward increasing the solar to fuel efficiency of prototype devices. Within this context, we describe a study on the growth of wurtzite indium phosphide (InP) nanowire (NW) arrays on silicon substrates and their subsequent implementation as light-absorbing photocathodes in PEC cells. The high onset potential (0.6 V *vs* the reversible hydrogen electrode) and photocurrent (18 mA/cm^2) of the InP photocathodes render them as promising building blocks for high performance PEC cells. As a proof of concept for overall system integration, InP photocathodes were combined with a nanoporous bismuth vanadate ($BiVO_4$) photoanode to generate an unassisted solar water splitting efficiency of 0.5%.**

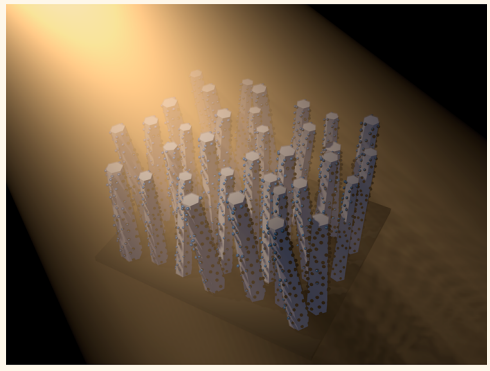

KEYWORDS: *nanowire synthesis, energy conversion, photoelectrochemistry, catalysis, chemical vapor deposition*

Increasing fossil fuel consumption and the resulting environmental damage have propelled many efforts in clean energy research. Solar power is among the most promising of such clean and renewable energy sources. However, due to the intermittent nature of sunlight and the temporal mismatch between solar energy flux and peak power consumption, a method for capturing and transforming sunlight into an energy dense storage medium must be realized. To this end, photoelectrochemistry (PEC) offers a potential avenue of doing so by using solar power to split water into oxygen and hydrogen, which can subsequently be used as an energy storage medium, fuel source, or chemical feedstock.[1]

One promising strategy toward PEC solar fuel generation is the utilization of a Z-scheme method.[2−11] This is a biomimetic approach that simulates photosynthetic systems consisting of a tandem, dual absorber configuration (Figure 1A). The primary advantages of using two separate light absorbers to carry out the reduction and oxidation reactions include (1) each light absorber is required to possess appropriate band edge positions only for the relevant hydrogen evolution reaction (HER) or oxygen evolution reaction (OER), (2) each light absorber needs to be stable only under the reducing or oxidizing conditions that it operates, (3) the voltage required to split water (practically ∼1.7 V) can be provided by the combination of the two light absorbers, and (4) the band gaps for the light absorbers can be selected to efficiently take advantage of separate parts of the solar spectrum, thus enabling a higher solar to fuel efficiency compared to using only a single light absorber.[3,12]

A multicomponent Z-scheme PEC cell can be treated as a modular system in which each building block (light absorber,

Received: March 25, 2016
Accepted: April 28, 2016
Published: April 28, 2016

DOI: 10.1021/acsnano.6b02083
ACS Nano 2016, 10, 5525−5535

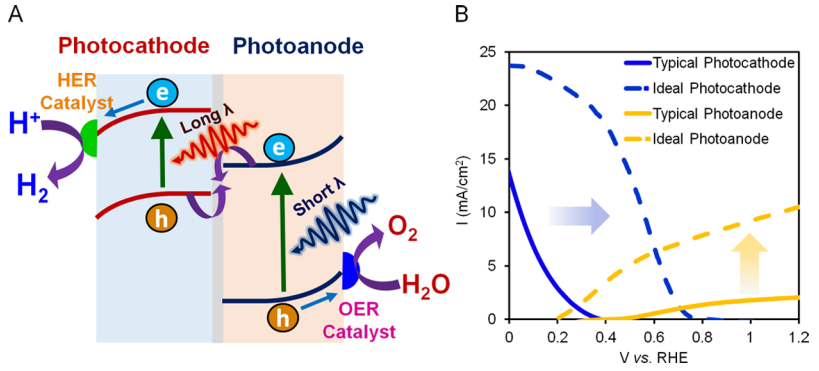

Figure 1. Modular Z-scheme PEC system is illustrated (A) in which individual light absorber and catalyst components can be systematically improved before reintegrating into the overall system. The performance of typical PEC integrated systems suffers from insufficient photocathode voltage and photoanode current (B). A protection layer (not shown) is occasionally present on the photocathode and/or photoanode surfaces.

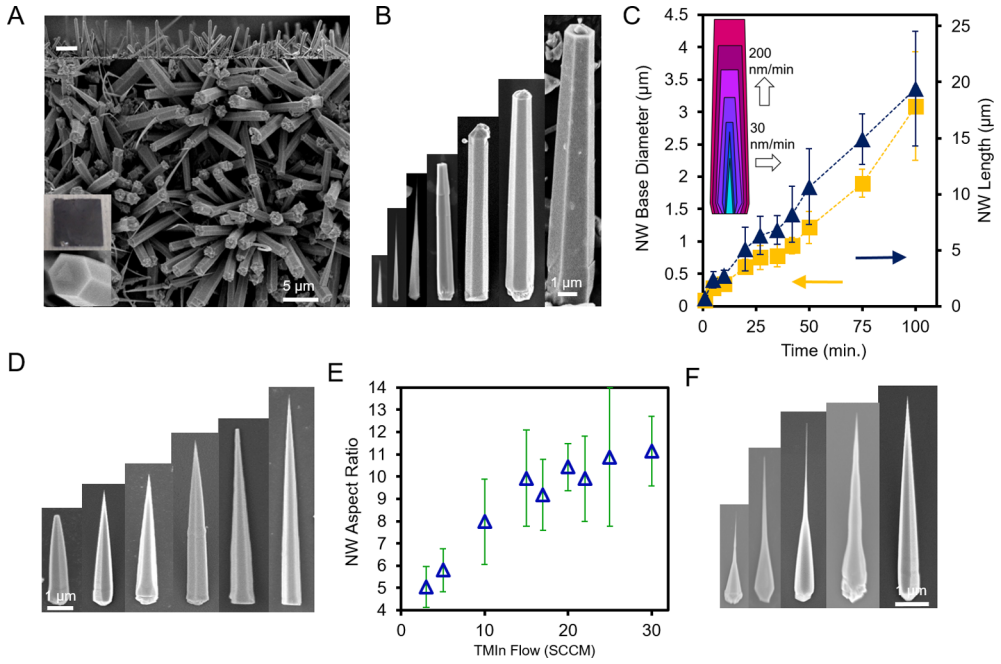

Figure 2. InP NW growth. A typical SEM top down (bottom) and cross-sectional view (top) of the resulting NW arrays (A). The insets depict a typical faceted NW tip and a 1 × 1 cm Si chip with an InP array. The NW length and diameter both increase linearly with growth time (B, C). Representative InP NWs under varied TMIn precursor flow from 3 to 20 SCCM (left to right) (D) and their aspect ratio statistics (E). InP NWs resulting from modification of TBP flow from 50 to 500 SCCM, left to right (F).

catalyst, electrolyte, membrane) can be individually modified, optimized and subsequently reintegrated to improve the device as a whole. One can estimate the efficiency of an integrated PEC system from the crossover of overlaid current−voltage (*I*−*V*) curves of the individual light absorber/catalyst components.[13] As illustrated in Figure 1B, the efficiency of conventional PEC systems typically suffers from a lack of photovoltage from commonly used photocathodes as well as from insufficient photocurrent from typical photoanodes. Within this context, the present work focuses on the development of an improved light-absorbing photocathode constituent. Indium phosphide (InP) is a promising candidate to replace commonly used silicon because it has a relatively narrow bandgap (1.35−1.42 eV) that can take advantage of a large portion of the incident solar spectrum and has been shown to exhibit exceptionally high voltages in PEC half cells.[14−17] The typically high carrier mobility and low surface recombination velocity of this material are beneficial for efficient charge separation and catalysis.[18,19] Furthermore, only a small amount of InP is necessary to fully absorb incident solar radiation because of its direct band gap. Utilizing InP in the NW morphology offers the additional benefits of a high surface area for increased catalyst loading and decreased reflection of incident photons through light trapping effects.[20,21] Moreover, the growth of InP NW arrays on silicon substrates as opposed to the commonly used InP substrates can make InP NW-based photocathodes more practical for scale-up by minimizing cost and material consumption.

In the following sections, we detail a study on the growth of InP NWs on silicon substrates. Following synthetic and structural analysis, we tune the InP NW electronic character by incorporating zinc (Zn) as a p-type dopant and proceed to study the material's optical and electrochemical properties. We next photodeposit platinum (Pt) HER catalysts onto the NWs

DOI: 10.1021/acsnano.6b02083
ACS Nano 2016, 10, 5525−5535

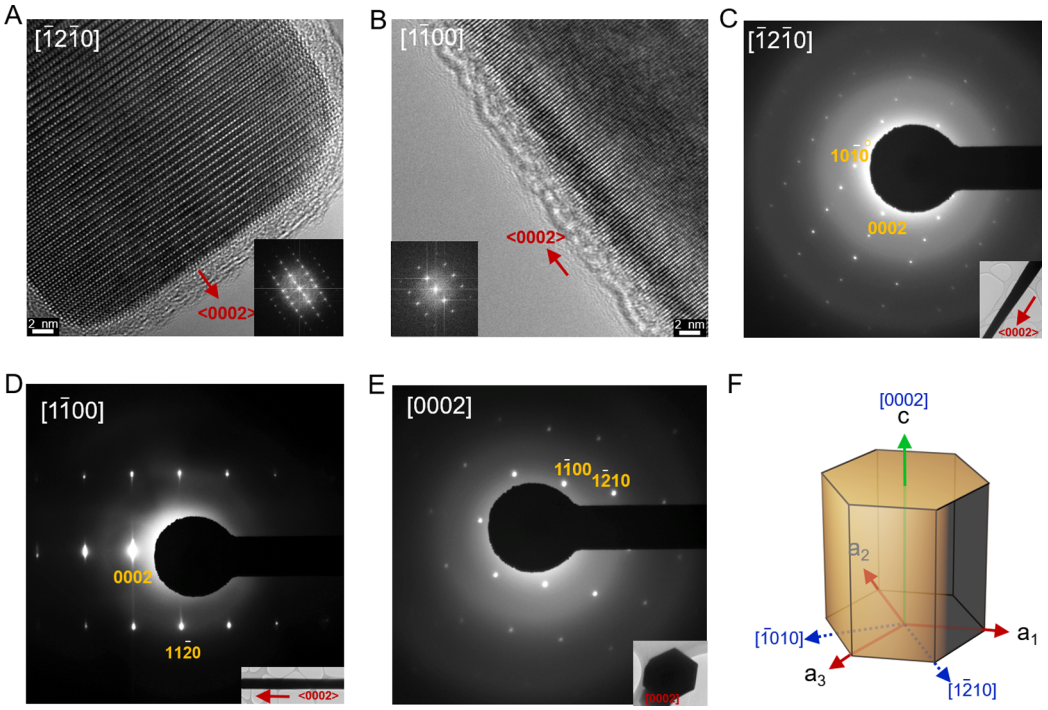

Figure 3. HRTEM (A,B) and electron diffraction (C−E) demonstrate that the InP NWs grow in the WZ phase with a ⟨0002⟩ growth direction, {1−100} side facets, and corners aligned with the {1−210} facets. Insets illustrate fast Fourier transforms of the HRTEM images in A, B, and low resolution TEM images of the NW from the electron diffraction images in C, D, E. A structural model is produced from the HRTEM and electron diffraction data showing surface facets and growth direction (F).

and utilize our InP photocathodes in both PEC half cells and in integrated water splitting systems with a bismuth vanadate ($BiVO_4$) photoanode.

RESULTS/DISCUSSION

Nanowire Growth. Indium phosphide has been previously synthesized using a variety of different methods, including solution phase synthesis,[22−26] phosphorization of indium films,[27,28] chemical vapor transport (CVT),[29,30] laser ablation,[31] and chemical vapor deposition (CVD).[32−43] In this work, we pursued the CVD method since its growth parameters can be precisely fine-tuned and it offers a path to directly grow InP NWs on a conductive substrate. Degenerately doped, p-type, ⟨111⟩ Si was chosen as a cost-effective conductive growth substrate. This type of silicon would minimize substrate PEC contribution and facilitate the InP majority carrier transport through the PEC circuit. Though an ∼8% lattice mismatch exists between InP and Si, InP NWs have been previously grown with success on ⟨111⟩ Si substrates.[33,36,44] In this particular project design, we aimed to obtain InP NWs that were long enough to absorb the majority of above band gap radiation and wide enough to support a full built-in interfacial electric field with moderate doping concentrations.

With these design principles in mind, we developed a self-catalyzed growth of InP NWs on ⟨111⟩ Si substrates with a metal−organic CVD (MOCVD) process incorporating trimethylindium (TMIn) and *tert*-butylphosphine (TBP) as indium and phosphorus precursors, respectively (Figure 2A). Detailed growth parameters are provided in the Experimental Methods section. We did not observe by scanning electron microscopy (SEM) an indium metal catalyst at the tip of the NW but rather a clean end-facet or a polycrystalline tip. The catalyst tip was likely either fully consumed during the growth or soon after the TMIn flow was turned off. Time-dependent growth analysis (Figure 2B,C) with 10 standard cubic centimeters per minute (SCCM) TMIn and 500 SCCM TBP precursor flows revealed that the growth begins with small needle-like structures that continually grow in the axial and radial directions linearly with time to generate larger, faceted NWs. By varying the growth time, the dimensions of the NWs can be tuned to span nearly 2 orders of magnitude in both the radial (0.03 to 3.08 μm) and axial (0.29 to 19.43 μm) dimensions.

Seeking to obtain a further understanding of the NW growth and to demonstrate an additional layer of synthetic tunability, we varied the TBP/TMIn ratio and studied the effects of this on the NW morphology. While keeping the TBP flow constant at 500 SCCM, we modified the TMIn flow and discovered that the primary effect was the modulation of the NW aspect ratio. Representative NWs from 20 min growth times utilizing TMIn flow rates of 3−30 SCCM are depicted in Figure 2D. The base diameter remained unchanged, whereas the axial growth rate increased with TMIn flow until nearly leveling out at flow rates of 15 SCCM (Figure 2E). This indicates that the TMIn component was crucial for axial growth. A TMIn flow is likely necessary to maintain a liquid indium catalyst at the growing NW tip and the presence of this catalyst accelerates the axial growth rate. The constant base diameter over the entire experimental TMIn flow range points to the TMIn component as not being the limiting factor for the sidewall growth rate under these conditions.

Next, while holding the TMIn flow constant at 15 SCCM, we decreased the TBP flow from 500 to 50 SCCM (Figure 1F, right to left). Here, we discovered unusually shaped NWs that had a wide base yet terminated with a very thin (∼20 nm) end section. Although the TMIn was crucial for axial growth, under these synthetic conditions, TBP flow dictates radial growth

DOI: 10.1021/acsnano.6b02083
ACS Nano 2016, 10, 5525−5535

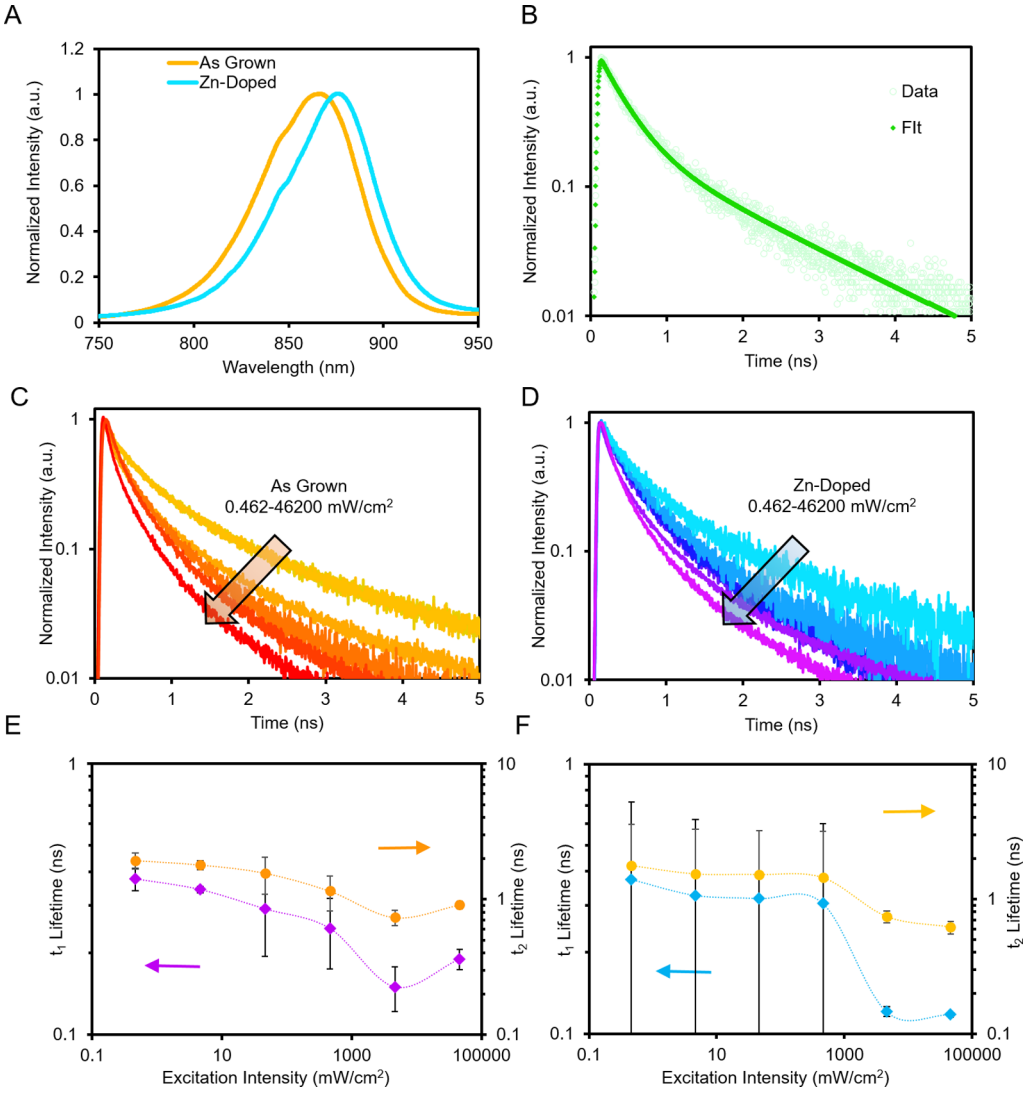

Figure 4. Optical measurements of InP. Steady state PL emission is slightly red-shifted for Zn-doped NWs relative to as-grown NWs (A). The PL lifetimes of NWs can be fit to a biexponential decay (B) in the case of as-grown as well as Zn-doped NWs. Both as-grown (C) and Zn-doped (D) NWs exhibit a decrease in PL lifetime with increasing excitation power. In contrast, the as-made NWs show far less heterogeneity in their lifetime distributions (E) relative to the Zn-doped NWs (F). t_1 and t_2 denote the fast and slow components in the photoluminescence decay. Error bars represent one standard deviation from 3 and 8 samples for undoped and zn-doped NWs, respectively.

dynamics with sidewall growth initially occurring at the base of the NW. These experiments together support a dual growth mechanism, consisting of self-catalyzed axial growth in conjunction with uncatalyzed epitaxial sidewall growth. In a TBP-deficient regime, radial sidewall growth proceeds by beginning at the base of the NWs and is outpaced by the axial growth. A similar phenomenon was observed with InGaAs nanostructures in which a lower *tert*-butylarsine precursor flow resulted in asymmetric structures with a wide base and a thin needle-like tip.[45] Here, the authors attributed this to a result of increased group III adatom diffusion lengths under low group V precursor flows and, as a result, faster axial growth rates. It should be noted that the growth of InP NWs presented here is not confined to ⟨111⟩ silicon substrates; InP NWs were also successfully grown on ⟨100⟩ silicon, gallium nitride, and molybdenum substrates (Figure S2).

Structural Characterization. We next utilized microscopic characterization methods to determine the crystallographic phase of the InP NWs. High resolution transmission electron microscopy (HRTEM) images (Figure 3A,B) taken perpendicular to the [−12−10] and [1−100] zone axes reveal that the InP NWs grow in the wurtzite (WZ) phase with a ⟨0002⟩ growth direction. Electron diffraction images (Figure 3 C-E) from the InP NWs aligned to the [−12−10], [1−100] and [0002] axes indicate that the hexagonal NWs have facets perpendicular to the {1−100} axes and edges perpendicular to the {1−210} axes. From the comprehensive crystallographic measurements, a structural model is derived (Figure 3F). X-ray diffraction (XRD) was utilized as a macroscopic structural measurement. The WZ phase was the primary contribution to the XRD spectrum, although a zincblende (ZB) component is also present (Figure S3). This is likely due to a layer of InP ZB particles on the substrate that grow in conjunction with the NWs as well as from the NW tips, which occasionally terminate with a polycrystalline ZB layer.

InP adopts the ZB phase in the bulk but the WZ phase is commonly observed in InP nanostructures. This can be rationalized by the high surface to volume ratio of

DOI: 10.1021/acsnano.6b02083
ACS Nano 2016, 10, 5525−5535

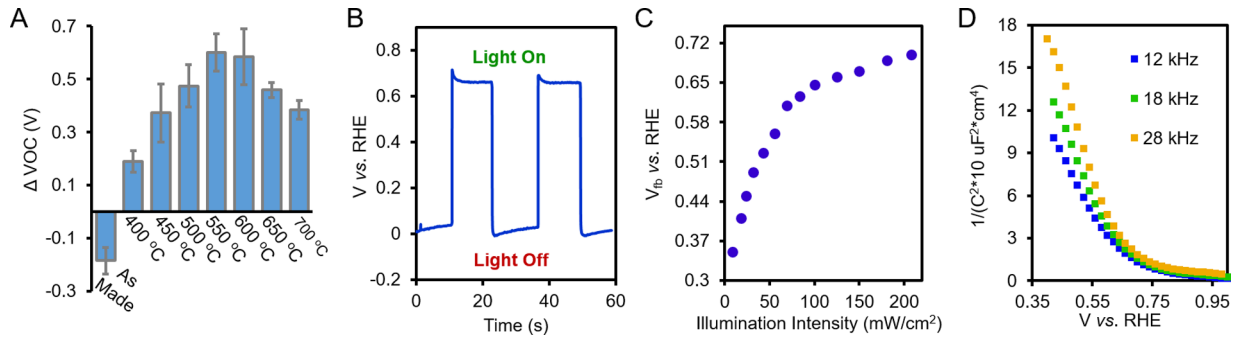

Figure 5. Flat band potential measurements. InP doped at 550 °C shows the highest open circuit photovoltage (A). A typical open circuit photovoltage plot is illustrated in (B). The flat band potential measured through OCP does not change much with illumination intensity after 100 mW/cm^2, indicating that the measured value is close to the true flat band potential (C). Furthermore, Mott−Schottky measurements yield a flat band potential of ∼0.7 V *vs* RHE, which is consistent with OCP measurements (D).

nanostructures; ZB is the thermodynamically preferred phase in the bulk but WZ has a lower surface energy due to a smaller density of surface dangling bonds.[37] Hence, InP NWs with diameters less than 25 nm typically adopt the WZ phase. Because the growth of our NWs initiates with thin needle-like seeds and proceeds to grow in an epitaxial fashion, the WZ phase is not unexpected. Beyond the initial stages of growth, the NWs are likely trapped in a metastable regime in which the WZ is no longer the lowest energy phase but a large energy input would be required to transform the crystal to the ZB phase.

An additional parameter that affects the resulting crystallographic phase of InP NWs is the V/III precursor ratio, with higher ratios commonly leading to the WZ phase.[46−50] This phenomenon has previously been exploited to gain precise crystallographic control of III−V NWs and to even grow periodically twinned NWs.[41] In these cases, the preferred formation of the WZ phase was attributed to effects of varied growth kinetics, catalyst supersaturation, surface energies, and precursor mass transport limitations. Often, high V/III precursor ratios lead to the WZ phase; our resulting NWs are grown with a typical V/III ratio of ∼1000, thus the WZ phase is expected.

Zinc Doping. Following the growth and structural studies, we proceeded to develop photocathodes from the InP NWs. For all subsequent studies, InP NWs with 15 SCCM TMIn, 500 SCCM TBP, and 20 min growth times were used. Because InP grows inherently n-type as a result of phosphorus vacancies and oxygen impurities, it is critical to introduce a p-type acceptor to render InP suitable for photocathode fabrication.[51−53] Zn was chosen as a p-type substitutional dopant because its ionization potential lies near the InP valence band, and it is the most commonly studied InP p-type dopant.[54] The as-grown InP NWs were doped with Zn *via* a thermal diffusion (400−700 °C for 1 h under 10% H_2/Ar) process using zinc phosphide both as a source of Zn and to maintain a phosphorus rich atmosphere during the doping process.[14] We note that the actual local temperature of the InP and Zn source is likely to be substantially lower than the set point of the tube furnace heat source. Further details are presented in the Experimental Methods section.

Optical Characterization. Steady-state photoluminescence (PL) and time-resolved photoluminescence (TRPL) measurements were performed on the as-grown and Zn-doped NWs. For this section, NWs doped with Zn at 550 °C were measured since they were found to exhibit optimal electrochemical properties. Steady state PL spectroscopy of as-grown InP NWs reveals that they emit at a wavelength of ∼862 nm (1.44 eV) (Figure 4A). In addition to the primary emission peak, a lower energy shoulder is present. This phenomenon is consistent with previous measurements of InP in the WZ phase and is attributed to valence band splitting in the band structure.[55−59] Zn-doped NWs feature a red-shifted emission at ∼878 nm (1.41 eV). A possible explanation for this could be radiative emission from a donor−acceptor transition.[60]

To further probe the optical properties of both types of NWs, we examined their PL emission *via* time-resolved measurements. We measured the lifetime of the NWs across 6 orders of magnitude of excitation intensity. The purpose of this was to glean information about the excited state recombination dynamics. For both types of NWs, the PL decay curves could be fit with a biexponential decay pattern (Figure 3B). Biexponential decays in semiconductor materials typically indicate the presence of a faster defect or surface related component and a band to band recombination component. In our case, the fast component typically contributed to 70−80% of the data, whereas the slow component contributed to 20−30% of the decay curve.

As excitation intensity is increased from 0.462 to 46200 mW/cm^2, the lifetime of both components decreased (Figure 3C,D), providing evidence that in this regime, traps (likely due to surface states and crystallographic defects) are already filled and multielectron processes are accelerating recombination kinetics. In addition, the as-grown NWs show consistent behavior, whereas Zn-doped NWs exhibit a much larger spread (Figures 4E,F and S4) in their lifetime values. This variation of optical properties is likely a result of the high temperature annealing in a Zn and P rich environment and may stem from the addition or elimination of various defects that may vary from wire to wire. This result indicates that the homogeneity of the NWs through the doping process could be improved and the effects of optical heterogeneity on the overall device performance remain an open question.

Flat Band Potential Measurement. In this section, we examine the effects of Zn doping on the flat band potential of the InP NWs using open circuit photovoltage (OCP) and Mott−Schottky measurements. The flat band potential and interfacial band bending of the InP NWs were optimized by varying the temperature of the thermal diffusion Zn doping process. At elevated temperatures, Zn diffuses rapidly through the InP lattice.[61,62] Therefore, the primary factor that controlled the resulting concentration of Zn in the InP lattice

DOI: 10.1021/acsnano.6b02083
ACS Nano 2016, 10, 5525−5535

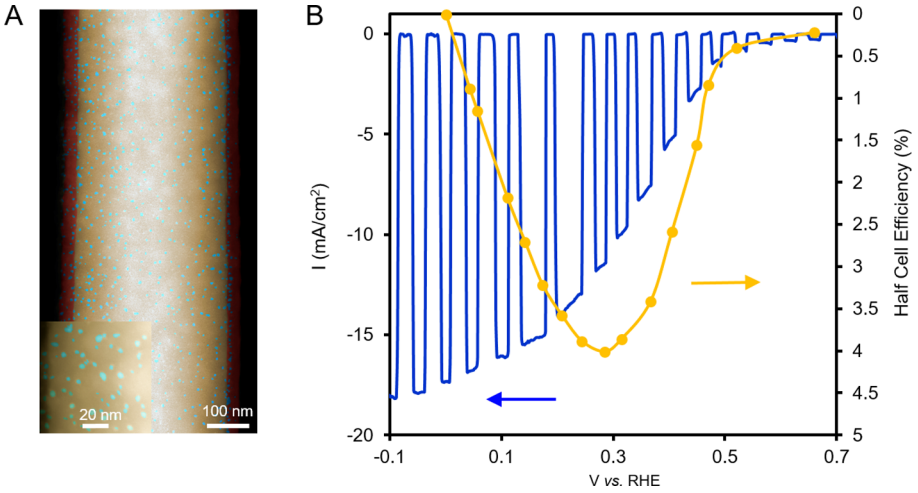

Figure 6. False color STEM image of an InP NW (yellow), TiO_2 shell (red), and Pt nanoparticle cocatalysts (blue) (A). Current−voltage curve of InP photocathode indicates a maximum half-cell efficiency of 4% (B).

was the temperature dependent partial pressure of gaseous Zn.[63] OCP measurements were first utilized to test the degree of band bending at the InP surface after the doping process. Briefly, after the ZnP thermal diffusion, an atomic layer deposition (ALD) titanium dioxide (TiO_2) layer was deposited onto the NW surface as a protection layer. The TiO_2 acts as a protection layer and an electron selective contact and is commonly used with InP photocathodes.[14,15,64] The InP/TiO_2 heterostructure features type II band alignment. The majority of the band bending occurs at InP at this interface, which is subsequently probed. Following the TiO_2 deposition, an indium−gallium eutectic was used to make an ohmic contact to the backside of the Si chip. In a three-electrode setup with a carbon foil counter and Ag/AgCl reference electrode, the working electrode potential was measured under dark and under one-sun illumination.

When the InP electrode is illuminated at open circuit, electrons from the valence band are promoted to the conduction band, are driven to and build up at the semiconductor-electrolyte interface, leading to a splitting of quasi-Fermi levels of electrons ($E_{F,e}$) and holes ($E_{F,h}$) (Figure 5C). The degree of quasi-Fermi-level splitting is measured by the change in the working electrode voltage under light and dark conditions. This is an estimate of the attainable photovoltage under PEC operating conditions.[65,66]

When considering the optimal doping level for our NW electrodes, of importance was to achieve a high enough doping level to support a full built-in electric field (i.e., not depleted through the entire NW diameter), without introducing an excessive amount of defects. Excess defects can act as recombination centers and decrease the photovoltage. The depletion width, W, is defined for a one-dimensional interface by

$$W = \sqrt{\frac{2\varepsilon\varepsilon_0 \Delta V}{eN_d}}$$

where ε_0 is vacuum permittivity, ε is the InP dielectric constant, ΔV is the potential difference between InP and the redox couple in solution or Fermi level of a semiconductor in the case of a heterostructure and the InP Fermi level, e is the elementary charge and N_d is the carrier concentration. At insufficient carrier concentrations W is larger than the NW radius and a full built-in electric field cannot be supported. W is plotted as a function of N_d (Figure S5) and the results indicate that for a NW 500 nm in diameter, a N_d of at least $10^{16}/cm^3$ is required. A series of systematic OCP measurements as a function of ZnP annealing temperature were performed (Figure 5A). Undoped InP displayed a negative OCP, indicating an upward band bending at equilibrium and likely an initial n-type character. The OCP was positive across our experimental range of annealing temperatures (400−700 °C), maximizing at 550 °C until decreasing again. This is likely explained by the following: the NWs annealed at lower temperatures (400−450 °C) are still fully depleted across their diameter. At optimal annealing temperatures (500−600 °C) the InP has an optimum carrier concentration and is no longer fully depleted. Higher temperature annealing (650−700 °C) leads to an increase in defects, through either excessive Zn incorporation or through thermal degradation, and OCP is likely reduced through defect-induced recombination. These results would estimate that the optimized InP NWs have a carrier concentration in the range of 10^{16}−$10^{17}/cm^3$.

An OCP plot from an optimized InP photocathode annealed at 550 °C is presented in Figure 5B. At open circuit conditions, the electrochemical potential is at equilibrium with the primary redox couple in the acidic solution (H^+/H_2) at ∼0 V *vs* RHE. Upon illumination and subsequent quasi-Fermi level splitting the measured voltage increases to ∼0.65 V *vs* RHE. This can be viewed functionally as where the InP NWs can begin to generate a photocurrent. To determine whether this OCP measurement is close to the true value of the flat band potential, we measured the OCP as a function of illumination intensity. As presented in Figure 5C, the OCP initially increases with increasing illumination intensity until 100 mW/cm², indicating that in this region, the OCP is likely dominated by the effects of nonradiative recombination. At illumination intensities higher than 100 mW/cm², the OCP increases at a much lower rate. This is evidence that at quasi-static equilibrium, the trap states are mostly filled, and the quasi-Fermi level splitting is nearly maximized and thus approaches the true flat band potential.

The flat band potential was also independently measured *via* Mott−Schottky measurements. This particular technique measures the capacitance of the space-charge region (C_{sc}) in

DOI: 10.1021/acsnano.6b02083
ACS Nano 2016, 10, 5525−5535

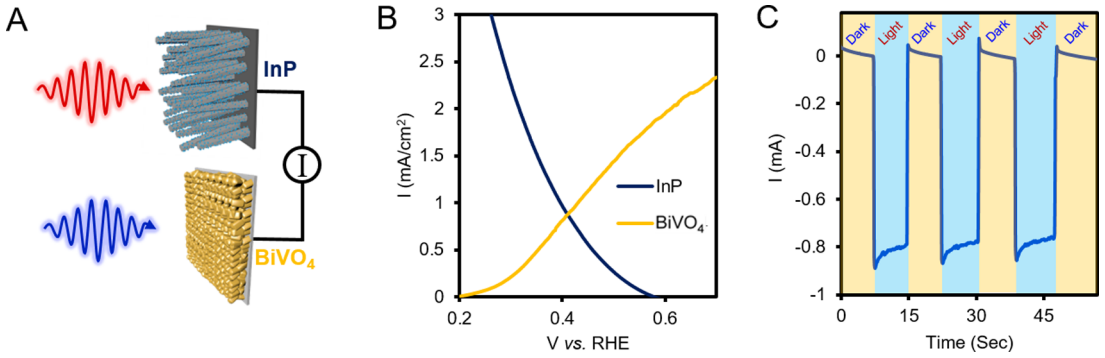

Figure 7. Overall water splitting. Schematic of InP/$BiVO_4$ tandem setup (A). The crossover in the current−voltage curves (B) is an estimate of the photocurrent generated from unassisted water splitting. In a two optical path configuration, ~0.8 mA photocurrent is generated without an applied bias (C).

the dark under a range of applied potentials.[67] In an ideal system, the C_{sc} obeys the relationship

$$\frac{1}{C_{sc}^2} = \frac{2}{\varepsilon\varepsilon_0 A^2 e N_d}\left(E - E_{fb} - \frac{kT}{e}\right)$$

where A is the area of the semiconductor-electrolyte interface, N_d is the carrier concentration, E is the applied potential, E_{fb} is the flat band potential, and k is the Boltzmann constant. The Mott−Schottky plot for our optimized InP photocathodes in a commonly used frequency range for this material is depicted in Figure 5D. The flat band potential can be measured and is determined to be at ~0.7 V *vs* RHE. Importantly, this value converges with the flat band value measured through OCP measurements, providing confidence that we are indeed recording the C_{sc} in this measurement. This flat band potential falls within the 0.6 to 1.1 V range typically measured for InP cathodes.[14−16,64,68−70] Although a fully quantitative determination of carrier concentration is not possible due to uncertainties in the absolute area and the variability of slope under different frequencies, the carrier concentration in the InP was roughly estimated using double layer capacitance to record the surface area and was found to be in the range of ~2−8 × 10^{16}/cm^3 (Figure S7). Additional improvements in maximizing photovoltage and flat band potential can potentially be made through modification of the TiO_2 ALD process, minimizing crystallographic defect density, or introducing built-in junctions through surface modification; these efforts may be pursued in future works.[14,43,71−73]

Photoelectrochemical Half-Cell Performance. After optimizing the doping procedure through OCP measurements, the InP NW photocathode's photoelectrochemical performance was tested. First, platinum nanoparticles were photodeposited from a solution of Pt salt dissolved in a water−methanol mixed solvent (see Experimental Methods section for details). After optimization, this method yielded a well-dispersed coating of ~5.4 ± 1.9 nm Pt particles on the InP surface (Figures 6A and S8). The Pt-loaded InP photocathode performance was then measured under chopped illumination in an acidic electrolyte (Figure 6B). Out of 11 devices tested under these conditions, the average current density at 0 V *vs* RHE was recorded to be 15.2 ± 2.0 mA/cm^2. The onset potential of ~0.6 V *vs* RHE is in good agreement with the flat band potential measured through OCP and Mott−Schottky measurements. Quantitative gas product measurement was utilized to confirm that the origin of this photocurrent primarily stemmed from H_2 production (Figure S9). One metric used to quantify photocathode performance is the half-cell efficiency. The efficiency, depicted as η, was calculated through

$$\eta = \frac{1.23 \times (\text{V } vs \text{ RHE}) \times I(\text{mA/cm}^2)}{P_{incident}} \times 100\%$$

where $P_{incident}$ was 100 mW/cm^2. Although the actual device efficiency will depend on the photoanode performance, among other variables, this metric is useful for comparing to other photocathodes in the literature. The half-cell efficiency of our InP photocathode (Figure 6B) of 4.0% is comparable to that of InP NWs grown on InP substrates, indicating that using low-cost Si growth substrates may be a promising avenue for further development of such photocathodes.[16] However, this half-cell efficiency was still lower than record InP devices, indicating that there is room for further improvement.[15]

The InP photocathode's current voltage and stability curves were also tested in neutral and basic electrolytes (Figure S10). In neutral and basic electrolytes, the InP fill factor was not as high as that of the InP in acidic conditions, likely due to differences in surface catalysis kinetics. Chronoamerometric scans of the InP in all three conditions were tested through chronoamperometric measurements over the span of 10 h or more. The photocurrent typically decayed to 50−70% of its initial value before stabilizing. Further improvements can be made by developing and enhancing the protection layer and catalyst adhesion.

Overall Water Splitting. To explore the prospects for InP NWs as building blocks in integrated water splitting systems, we sought to combine the InP photocathode with a light-absorbing photoanode to generate a proof of concept system. We chose bismuth vanadate ($BiVO_4$) as the photoanode component as it has recently been demonstrated to function efficiently in a half cell configuration. Furthermore, $BiVO_4$ can absorb photons with energies greater than 2.4 eV, rendering it promising to both spectrally match with low band gap semiconductor photocathodes and also attain a maximum photocurrent density of 7.5 mA/cm^2. This is not possible with high band gap photoanodes such as TiO_2.[3] We fabricated $BiVO_4$ photoanodes coated with a CoPi oxygen evolution catalyst according to a previously published procedure.[74−76]

Due to the lack of stability of $BiVO_4$ in acidic conditions, the InP−$BiVO_4$ tandem was tested in neutral pH. In this experiment, a two optical path configuration was utilized as a result of the high degree of light scattering of the $BiVO_4$ electrode (Figure 7A). The half-cell photocurrent curves of InP and $BiVO_4$ electrodes under the same operating conditions are

DOI: 10.1021/acsnano.6b02083
ACS Nano 2016, 10, 5525−5535

plotted in Figure 7B. The crossover at ~0.85 mA/cm^2 indicates that this magnitude of unassisted water-splitting current should be attainable in a two electrode configuration. Indeed, under illumination the InP−$BiVO_4$ tandem system generates 0.82 ± 0.04 mA per two electrodes with an area of 1 cm^2 each, corresponding to a solar to fuel efficiency of 0.5%. Although this efficiency is ~4 times the magnitude of our previous Si/TiO_2 tandem system, there is still much room to improve.[3] Aside from the continued development of the InP photocathodes, future work will include utilizing photoanodes with higher photocurrent at more negative potentials and increased sub-band-gap transmission that will allow for one optical path (Figure S15) to be used.[77]

CONCLUSIONS

In this study, we developed the growth and application of InP NWs as the light-absorbing photocathode component of PEC cells. The growth of InP NWs was found to proceed *via* both a self-seeded axial growth and a radial epitaxial growth. This resulted in WZ phase InP NWs whose geometry can be readily tuned over 2 orders of magnitude. Their integration on Si substrates renders them promising for potential scale-up applications. To utilize the InP NWs as photocathodes, we doped them with Zn. The optimized NWs exhibit a 4.0% light to hydrogen efficiency in a half-cell configuration. When combined with a light-absorbing photoanode in a tandem system, a 0.5% overall water splitting efficiency can be achieved. The present work represents the initial development of WZ InP NWs on silicon with many promising avenues to further improve.

EXPERIMENTAL METHODS

Nanowire Growth. InP NWs were grown primarily on Si ⟨111⟩ chips, degenerately p-type doped (~0.001Ω/cm). Prior to growth, the Si chips were cleaned by sonication in acetone, followed by isopropyl alcohol, then water for 10 min in each solvent. The Si chips were then immersed in a 6:1 buffered oxide etch to remove the native oxide layer and briefly dipped into a lactate solution for further impurity removal. The InP NWs were grown in a Thomas Swann 1 × 3 CCS MOCVD. All growth occurred under a 75 Torr hydrogen environment. Prior to growth, the substrates were heated to 520 °C and TBP was flowed through for 3 min at 500 SCCM (2331 μmol/min). Following the TBP treatment, the substrates were cooled to 520 °C and TMIn and TBP were flown through for the desired time. The typical flow rates were 15 SCCM TMIn (2.5 μmol/min) and 500 SCCM TBP. Following the growth, the InP NWs were cooled to room temperature under a TBP flow of 100 SCCM. A growth schematic is depicted in Figure S1.

$BiVO_4$ Synthesis. $BiVO_4$ synthesis was performed in accordance to a previous report to produce nanoporous $BiVO_4$ on fluorine-doped tin oxide (FTO) coated glass slides.[74] First a precursor solution of 0.04 M $Bi(NO_3)_3$ and 0.4 M KI at pH 1.7 was prepared. Next, benzoquinone dissolved in ethanol was added to the solution. From this solution, a BiOI film was cathodically deposited onto an FTO electrode at 0.1 V *vs* Ag/AgCl for 20 min (Figures S10 and S11). Following the BiOI deposition, a small amount of DMSO containing 0.2 M $VO(acac)_2$ was drop-cast onto the BiOI-coated FTO electrode. The electrodes were next annealed at 450 °C for 2 h to convert the BiOI into $BiVO_4$. After annealing, the excess vanadium precursor was removed through a brief soak in 1 M NaOH. Prior to PEC testing, an amorphous cobalt phosphate catalyst was photoelectrochemically deposited (60 s. at 1.3 V *vs* Ag/AgCl) in a pH 7, 0.1 M potassium phosphate buffer containing 0.5 mM $Co(NO_3)_2$.

Atomic Layer Deposition. Amorphous titania films were deposited at 120 °C using $TiCl_4$ and water as titanium and oxygen precursors, respectively. A home-built thermal ALD was utilized to complete this process. Both precursors were held at room temperature. Nitrogen was used as both the purge gas and precursor carrier gas at a flow rate of 10 SCCM. Pulse times were 0.2 s for $TiCl_4$ and 0.1 s for water. The amorphous titania was deposited at a rate of 0.5 nm/cycle. Typically, 600 cycles were performed on the InP films to achieve a coating thickness of 30 nm.

Physical Characterization. The NW morphology was characterized with a JEOL 6340F FE SEM at an accelerating voltage of 5 kV. Low resolution TEM imaging and electron diffraction was performed with a Hitachi H-7650 TEM at an accelerating voltage of 120 kV. High resolution TEM imaging was performed with a FEI Tecnai F20 UT electron microscope operated at 200 kV accelerating voltage. High angle annular dark field scanning transmission electron microscopy images were acquired with a FEI TitanX microscope operated at 300 kV accelerating voltage. Image analysis such as particle size determination was carried out with Digital Micrograph and ImageJ software. Digital Micrograph software was used for processing of high resolution TEM images. X-ray diffraction spectra were collected using a Bruker D8 Advance diffractometer (Cu Kα, λ = 0.154 nm) and a Bruker D8 GAADS diffractometer (Co Kα, λ = 0.179 nm).

Zinc Doping. Doping with Zn was performed *via* thermal annealing using zinc phosphide powder as a source of zinc and to maintain a phosphorus rich atmosphere during the process. The InP NW/silicon chip was placed in a ceramic crucible 2 mm above the ZnP powder and covered with a glass lid, similar to a sublimation furnace configuration. A slow flow of 10% H_2/Ar was maintained throughout the process.

Optical Characterization. All optical measurements were performed at room temperature. Steady state photoluminescence spectra were acquired with a Horiba Jobin-Yvon Labram HR confocal Raman system. An excitation wavelength of 532 nm was employed using a diode laser. TRPL measurements were performed with a PDM-50 avalanche photodiode input to a Picoharp300 time-correlated single photon counting module. The excitation source was the second harmonic (402 nm, 300 kHz, 150−200 fs) of a Coherent RegA amplifier seeded by a Coherent Mira oscillator.

Electrochemical and Photoelectrochemical Characterization. Electrochemical data were acquired using a Biologic VMP 300 potentiostat and EC Lab electrochemistry software. Typically, 1 M HCl was utilized as the acidic electrolyte, 1 M potassium phosphate buffer (pH 7) as a neutral electrolyte, and 1 M NaOH as the basic electrolyte. A 300 W xenon lamp with an AM 1.5G filter was used as the light source. The incident power on the electrode was measured using a calibrated silicon photodiode.

Platinum Photodeposition. Pt nanoparticles were photodeposited onto the photocathode surface. This was accomplished first by mixing a 4:1 solution of water:methanol containing 0.05 mM H_2PtCl_6. The photocathode was immersed in the solution and illuminated with 1 sun irradiation for 15 s. In this process, the Pt(IV) is reduced to elemental Pt particles on the surface with photogenerated electrons and the

DOI: 10.1021/acsnano.6b02083
ACS Nano 2016, 10, 5525−5535

photogenerated holes are quenched by oxidizing methanol. Following this, the photocathode was rinsed thoroughly with water and a linear sweep measurement was performed to reduce any leftover adsorbed Pt salts on the surface. This process was typically repeated three times.

Product Analysis. Hydrogen was measured with an Agilent 300 micro GC. A batch reactor setup was used with a home-built airtight photoelectrochemical cell. Oxygen was detected in real time using a NEOFOX-GT footprint phase fluorimeter coupled with an Ocean Optics oxygen sensor probe.

ASSOCIATED CONTENT

Supporting Information

The Supporting Information is available free of charge on the ACS Publications website at DOI: 10.1021/acsnano.6b02083.

Additional TEM analysis, electrochemical and photoelectrochemical measurements. (PDF)

AUTHOR INFORMATION

Corresponding Author

*E-mail: p_yang@berkeley.edu.

Notes

The authors declare no competing financial interest.

ACKNOWLEDGMENTS

This work was supported by the Physical Chemistry of Inorganic Nanostructures Program, KC3103, Office of Basic Energy Sciences of the United States Department of Energy under Contract No. DE-AC02-05CH11231. Electron microscopy was carried out at the National Center of Electron Microscopy (NCEM), which is supported by the Office of Science, Office of Basic Energy Sciences of the U.S. Department of Energy under Contract No. DE-AC02-05CH11231. Work at the Molecular Foundry was supported by the Office of Science, Office of Basic Energy Sciences of the U.S. Department of Energy under Contract No. DE-AC02-05CH11231. We thank Yude Su for help with optical data.

REFERENCES

(1) Lewis, N. S.; Nocera, D. G. Powering the Planet: Chemical Challenges in Solar Energy Utilization. *Proc. Natl. Acad. Sci. U. S. A.* **2006**, *103*, 15729−15735.

(2) Tachibana, Y.; Vayssieres, L.; Durrant, J. R. Artificial Photosynthesis for Solar Water-Splitting. *Nat. Photonics* **2012**, *6*, 511−518.

(3) Liu, C.; Tang, J.; Chen, H. M.; Liu, B.; Yang, P. A. Fully Integrated Nanosystem of Semiconductor Nanowires for Direct Solar Water Splitting. *Nano Lett.* **2013**, *13*, 2989−2992.

(4) Wang, Q.; Hisatomi, T.; Jia, Q.; Tokudome, H.; Zhong, M.; Wang, C.; Pan, Z.; Takata, T.; Nakabayashi, M.; Shibata, N. Scalable Water Splitting on Particulate Photocatalyst Sheets with a Solar-to-Hydrogen Energy Conversion Efficiency Exceeding 1%. *Nat. Mater.* **2016**, DOI: 10.1038/nmat4589.

(5) Prévot, M. S.; Sivula, K. Photoelectrochemical Tandem Cells for Solar Water Splitting. *J. Phys. Chem. C* **2013**, *117*, 17879−17893.

(6) Jiang, F.; Gunawan; Harada, T.; Kuang, Y.; Minegishi, T.; Domen, K.; Ikeda, S. Pt/In2s3/Cds/Cu2znsns4 Thin Film as an Efficient and Stable Photocathode for Water Reduction under Sunlight Radiation. *J. Am. Chem. Soc.* **2015**, *137*, 13691−13697.

(7) Lai, Y. H.; Palm, D. W.; Reisner, E. Multifunctional Coatings from Scalable Single Source Precursor Chemistry in Tandem Photoelectrochemical Water Splitting *Adv. Energy Mater.***2015**, *5*, 10.1002/aenm.201501668

(8) Liu, B.; Wu, C.-H.; Miao, J.; Yang, P. All Inorganic Semiconductor Nanowire Mesh for Direct Solar Water Splitting. *ACS Nano* **2014**, *8*, 11739−11744.

(9) Yang, H. B.; Miao, J.; Hung, S.-F.; Huo, F.; Chen, H. M.; Liu, B. Stable Quantum Dot Photoelectrolysis Cell for Unassisted Visible Light Solar Water Splitting. *ACS Nano* **2014**, *8*, 10403−10413.

(10) Bornoz, P.; Abdi, F. F.; Tilley, S. D.; Dam, B.; Van De Krol, R.; Graetzel, M.; Sivula, K. A. Bismuth Vanadate−Cuprous Oxide Tandem Cell for Overall Solar Water Splitting. *J. Phys. Chem. C* **2014**, *118*, 16959−16966.

(11) Jang, J.-W.; Du, C.; Ye, Y.; Lin, Y.; Yao, X.; Thorne, J.; Liu, E.; McMahon, G.; Zhu, J.; Javey, A.; Guo, J.; Wang, D. Enabling Unassisted Solar Water Splitting by Iron Oxide and Silicon. *Nat. Commun.* **2015**, *6*, 7447.

(12) Seitz, L. C.; Chen, Z.; Forman, A. J.; Pinaud, B. A.; Benck, J. D.; Jaramillo, T. F. Modeling Practical Performance Limits of Photoelectrochemical Water Splitting Based on the Current State of Materials Research. *ChemSusChem* **2014**, *7*, 1372−1385.

(13) Walter, M. G.; Warren, E. L.; McKone, J. R.; Boettcher, S. W.; Mi, Q.; Santori, E. A.; Lewis, N. S. Solar Water Splitting Cells. *Chem. Rev.* **2010**, *110*, 6446−6473.

(14) Lin, Y.; Kapadia, R.; Yang, J.; Zheng, M.; Chen, K.; Hettick, M.; Yin, X.; Battaglia, C.; Sharp, I. D.; Ager, J. W.; Javey, A. Role of TiO_2 Surface Passivation on Improving the Performance of P-InP Photocathodes. *J. Phys. Chem. C* **2015**, *119*, 2308−2313.

(15) Lee, M. H.; Takei, K.; Zhang, J.; Kapadia, R.; Zheng, M.; Chen, Y. Z.; Nah, J.; Matthews, T. S.; Chueh, Y. L.; Ager, J. W.; Javey, A. P-Type InP Nanopillar Photocathodes for Efficient Solar-Driven Hydrogen Production. *Angew. Chem.* **2012**, *124*, 10918−10922.

(16) Gao, L.; Cui, Y.; Wang, J.; Cavalli, A.; Standing, A.; Vu, T. T.; Verheijen, M. A.; Haverkort, J. E.; Bakkers, E. P.; Notten, P. H. Photoelectrochemical Hydrogen Production on InP Nanowire Arrays with Molybdenum Sulfide Electrocatalysts. *Nano Lett.* **2014**, *14*, 3715−3719.

(17) Heller, A.; Miller, B.; Lewerenz, H.; Bachmann, K. An Efficient Photocathode for Semiconductor Liquid Junction Cells: 9.4% Solar Conversion Efficiency with P-InP/Vcl3-Vcl2-Hcl/C. *J. Am. Chem. Soc.* **1980**, *102*, 6555−6556.

(18) Storm, K.; Halvardsson, F.; Heurlin, M.; Lindgren, D.; Gustafsson, A.; Wu, P. M.; Monemar, B.; Samuelson, L. Spatially Resolved Hall Effect Measurement in a Single Semiconductor Nanowire. *Nat. Nanotechnol.* **2012**, *7*, 718−722.

(19) Joyce, H. J.; Wong-Leung, J.; Yong, C.-K.; Docherty, C. J.; Paiman, S.; Gao, Q.; Tan, H. H.; Jagadish, C.; Lloyd-Hughes, J.; Herz, L. M.; Johnston, M. B. Ultralow Surface Recombination Velocity in InP Nanowires Probed by Terahertz Spectroscopy. *Nano Lett.* **2012**, *12*, 5325−5330.

(20) Garnett, E.; Yang, P. Light Trapping in Silicon Nanowire Solar Cells. *Nano Lett.* **2010**, *10*, 1082−1087.

(21) Kelzenberg, M. D.; Boettcher, S. W.; Petykiewicz, J. A.; Turner-Evans, D. B.; Putnam, M. C.; Warren, E. L.; Spurgeon, J. M.; Briggs, R. M.; Lewis, N. S.; Atwater, H. A. Enhanced Absorption and Carrier Collection in Si Wire Arrays for Photovoltaic Applications. *Nat. Mater.* **2010**, *9*, 239−244.

(22) Kornienko, N.; Whitmore, D. D.; Yu, Y.; Leone, S. R.; Yang, P. Solution Phase Synthesis of Indium Gallium Phosphide Alloy Nanowires. *ACS Nano* **2015**, *9*, 3951−3960.

(23) Baek, J.; Allen, P. M.; Bawendi, M. G.; Jensen, K. F. Investigation of Indium Phosphide Nanocrystal Synthesis Using a High-Temperature and High-Pressure Continuous Flow Microreactor. *Angew. Chem.* **2011**, *123*, 653−656.

(24) Trentler, T. J.; Hickman, K. M.; Goel, S. C.; Viano, A. M.; Gibbons, P. C.; Buhro, W. E. Solution-Liquid-Solidgrowth of Crystalline III-V Semiconductors: An Analogy to Vapor-Liquid-Solid Growth. *Science* **1995**, *270*, 1791−1794.

(25) Fanfair, D. D.; Korgel, B. A. Bismuth Nanocrystal-Seeded III-V Semiconductor Nanowire Synthesis. *Cryst. Growth Des.* **2005**, *5*, 1971−1976.

(26) Yu, H.; Li, J.; Loomis, R. A.; Wang, L.-W.; Buhro, W. E. Two-*Versus* Three-Dimensional Quantum Confinement in Indium Phosphide Wires and Dots. *Nat. Mater.* **2003**, *2*, 517−520.
(27) Kapadia, R.; Yu, Z.; Hettick, M.; Xu, J.; Zheng, M. S.; Chen, C.-Y.; Balan, A. D.; Chrzan, D. C.; Javey, A. Deterministic Nucleation of InP on Metal Foils with the Thin-Film Vapor−Liquid−Solid Growth Mode. *Chem. Mater.* **2014**, *26*, 1340−1344.
(28) Kiriya, D.; Zheng, M.; Kapadia, R.; Zhang, J.; Hettick, M.; Yu, Z.; Takei, K.; Wang, H.-H. H.; Lobaccaro, P.; Javey, A. Morphological and Spatial Control of InP Growth Using Closed-Space Sublimation. *J. Appl. Phys.* **2012**, *112*, 123102.
(29) Tang, C.; Bando, Y.; Liu, Z.; Golberg, D. Synthesis and Structure of InP Nanowires and Nanotubes. *Chem. Phys. Lett.* **2003**, *376*, 676−682.
(30) Shen, G.; Bando, Y.; Liu, B.; Tang, C.; Golberg, D. Unconventional Zigzag Indium Phosphide Single-Crystalline and Twinned Nanowires. *J. Phys. Chem. B* **2006**, *110*, 20129−20132.
(31) Gudiksen, M. S.; Wang, J.; Lieber, C. M. Synthetic Control of the Diameter and Length of Single Crystal Semiconductor Nanowires. *J. Phys. Chem. B* **2001**, *105*, 4062−4064.
(32) Kobayashi, N. P.; Wang, S.-Y.; Santori, C.; Williams, R. S. Growth and Characterization of Indium Phosphide Single-Crystal Nanoneedles on Microcrystalline Silicon Surfaces. *Appl. Phys. A: Mater. Sci. Process.* **2006**, *85*, 1−6.
(33) Mårtensson, T.; Svensson, C. P. T.; Wacaser, B. A.; Larsson, M. W.; Seifert, W.; Deppert, K.; Gustafsson, A.; Wallenberg, L. R.; Samuelson, L. Epitaxial III-V Nanowires on Silicon. *Nano Lett.* **2004**, *4*, 1987−1990.
(34) Mårtensson, T.; Carlberg, P.; Borgström, M.; Montelius, L.; Seifert, W.; Samuelson, L. Nanowire Arrays Defined by Nanoimprint Lithography. *Nano Lett.* **2004**, *4*, 699−702.
(35) Mohan, P.; Motohisa, J.; Fukui, T. Controlled Growth of Highly Uniform, Axial/Radial Direction-Defined, Individually Addressable InP Nanowire Arrays. *Nanotechnology* **2005**, *16*, 2903.
(36) Ren, F.; Ng, K. W.; Li, K.; Sun, H.; Chang-Hasnain, C. J. High-Quality InP Nanoneedles Grown on Silicon. *Appl. Phys. Lett.* **2013**, *102*, 012115.
(37) Moewe, M.; Chuang, L. C.; Dubrovskii, V. G.; Chang-Hasnain, C. Growth Mechanisms and Crystallographic Structure of InP Nanowires on Lattice-Mismatched Substrates. *J. Appl. Phys.* **2008**, *104*, 044313.
(38) Gao, L.; Woo, R. L.; Liang, B.; Pozuelo, M.; Prikhodko, S.; Jackson, M.; Goel, N.; Hudait, M. K.; Huffaker, D. L.; Goorsky, M. S.; Kodambaka, S.; Hicks, R. F. Self-Catalyzed Epitaxial Growth of Vertical Indium Phosphide Nanowires on Silicon. *Nano Lett.* **2009**, *9*, 2223−2228.
(39) Novotny, C. J.; Yu, P. K. L. Vertically Aligned, Catalyst-Free InP Nanowires Grown by Metalorganic Chemical Vapor Deposition. *Appl. Phys. Lett.* **2005**, *87*, 203111.
(40) Krishnamachari, U.; Borgstrom, M.; Ohlsson, B.; Panev, N.; Samuelson, L.; Seifert, W.; Larsson, M.; Wallenberg, L. Defect-Free InP Nanowires Grown in [001] Direction on InP (001). *Appl. Phys. Lett.* **2004**, *85*, 2077.
(41) Algra, R. E.; Verheijen, M. A.; Borgström, M. T.; Feiner, L.-F.; Immink, G.; van Enckevort, W. J.; Vlieg, E.; Bakkers, E. P. Twinning Superlattices in Indium Phosphide Nanowires. *Nature* **2008**, *456*, 369−372.
(42) Kitauchi, Y.; Kobayashi, Y.; Tomioka, K.; Hara, S.; Hiruma, K.; Fukui, T.; Motohisa, J. Structural Transition in Indium Phosphide Nanowires. *Nano Lett.* **2010**, *10*, 1699−1703.
(43) Woo, R. L.; Xiao, R.; Kobayashi, Y.; Gao, L.; Goel, N.; Hudait, M. K.; Mallouk, T. E.; Hicks, R. Effect of Twinning on the Photoluminescence and Photoelectrochemical Properties of Indium Phosphide Nanowires Grown on Silicon (111). *Nano Lett.* **2008**, *8*, 4664−4669.
(44) Alouane, M. H.; Chauvin, N.; Khmissi, H.; Naji, K.; Ilahi, B.; Maaref, H.; Patriarche, G.; Gendry, M.; Bru-Chevallier, C. Excitonic Properties of Wurtzite InP Nanowires Grown on Silicon Substrate. *Nanotechnology* **2013**, *24*, 035704.
(45) Ng, K. W.; Ko, W. S.; Lu, F.; Chang-Hasnain, C. J. Metastable Growth of Pure Wurtzite Ingaas Microstructures. *Nano Lett.* **2014**, *14*, 4757−4762.
(46) Paiman, S.; Gao, Q.; Joyce, H.; Kim, Y.; Tan, H.; Jagadish, C.; Zhang, X.; Guo, Y.; Zou, J. Growth Temperature and V/III Ratio Effects on the Morphology and Crystal Structure of InP Nanowires. *J. Phys. D: Appl. Phys.* **2010**, *43*, 445402.
(47) Paiman, S.; Gao, Q.; Tan, H.; Jagadish, C.; Pemasiri, K.; Montazeri, M.; Jackson, H.; Smith, L.; Yarrison-Rice, J.; Zhang, X.; Zou, J. The Effect of V/III Ratio and Catalyst Particle Size on the Crystal Structure and Optical Properties of InP Nanowires. *Nanotechnology* **2009**, *20*, 225606.
(48) Plante, M.; LaPierre, R. Growth Mechanisms of Gaas Nanowires by Gas Source Molecular Beam Epitaxy. *J. Cryst. Growth* **2006**, *286*, 394−399.
(49) Glas, F.; Harmand, J.-C.; Patriarche, G. Why Does Wurtzite Form in Nanowires of III-V Zinc Blende Semiconductors? *Phys. Rev. Lett.* **2007**, *99*, 146101.
(50) Joyce, H. J.; Wong-Leung, J.; Gao, Q.; Tan, H. H.; Jagadish, C. Phase Perfection in Zinc Blende and Wurtzite III− V Nanowires Using Basic Growth Parameters. *Nano Lett.* **2010**, *10*, 908−915.
(51) Alatalo, M.; Nieminen, R.; Puska, M.; Seitsonen, A.; Virkkunen, R. Phosphorus Vacancy in InP: A Negative-U Center. *Phys. Rev. B: Condens. Matter Mater. Phys.* **1993**, *47*, 6381.
(52) Mishra, R.; Restrepo, O. D.; Kumar, A.; Windl, W. Native Point Defects in Binary InP Semiconductors. *J. Mater. Sci.* **2012**, *47*, 7482−7497.
(53) Seitsonen, A.; Virkkunen, R.; Puska, M.; Nieminen, R. Indium and Phosphorus Vacancies and Antisites in InP. *Phys. Rev. B: Condens. Matter Mater. Phys.* **1994**, *49*, 5253.
(54) Benzaquen, M.; Belache, B.; Blaauw, C.; Bruce, R. Electrical Characteristics of Zinc-Doped Indium Phosphide. *J. Appl. Phys.* **1990**, *68*, 1694−1701.
(55) Li, K.; Ng, K. W.; Tran, T.-T. D.; Sun, H.; Lu, F.; Chang-Hasnain, C. J. Wurtzite-Phased InP Micropillars Grown on Silicon with Low Surface Recombination Velocity. *Nano Lett.* **2015**, *15*, 7189−7198.
(56) Li, K.; Sun, H.; Ren, F.; Ng, K. W.; Tran, T.-T. D.; Chen, R.; Chang-Hasnain, C. J. Tailoring the Optical Characteristics of Microsized InP Nanoneedles Directly Grown on Silicon. *Nano Lett.* **2013**, *14*, 183−190.
(57) Gao, Q.; Saxena, D.; Wang, F.; Fu, L.; Mokkapati, S.; Guo, Y.; Li, L.; Wong-Leung, J.; Caroff, P.; Tan, H. H.; Jagadish, C. Selective-Area Epitaxy of Pure Wurtzite InP Nanowires: High Quantum Efficiency and Room-Temperature Lasing. *Nano Lett.* **2014**, *14*, 5206−5211.
(58) Tuin, G. L.; Borgström, M. T.; Trägårdh, J.; Ek, M.; Wallenberg, L. R.; Samuelson, L.; Pistol, M.-E. Valence Band Splitting in Wurtzite InP Nanowires Observed by Photoluminescence and Photoluminescence Excitation Spectroscopy. *Nano Res.* **2011**, *4*, 159−163.
(59) De, A.; Pryor, C. E. Predicted Band Structures of III-V Semiconductors in the Wurtzite Phase. *Phys. Rev. B: Condens. Matter Mater. Phys.* **2010**, *81*, 155210.
(60) Moon, Y.; Si, S.; Yoon, E.; Kim, S. J. Low Temperature Photoluminescence Characteristics of Zn-Doped InP Grown by Metalorganic Chemical Vapor Deposition. *J. Appl. Phys.* **1998**, *83*, 2261−2265.
(61) Tuck, B.; Hooper, A. Diffusion Profiles of Zinc in Indium Phosphide. *J. Phys. D: Appl. Phys.* **1975**, *8*, 1806.
(62) Chang, L.; Casey, H. Diffusion and Solubility of Zinc in Indium Phosphide. *Solid-State Electron.* **1964**, *7*, 481−485.
(63) Schoonmaker, R. C.; Venkitaraman, A.; Lee, P. K. The Vaporization of Zinc Phosphide. *J. Phys. Chem.* **1967**, *71*, 2676−2683.
(64) Hettick, M.; Zheng, M.; Lin, Y.; Sutter-Fella, C. M.; Ager, J. W.; Javey, A. Non-Epitaxial Thin-Film InP for Scalable and Efficient Photocathodes. *J. Phys. Chem. Lett.* **2015**, *6*, 2177−2182.
(65) Chen, Z.; Dinh, H. N.; Miller, E. *Photoelectrochemical Water Splitting: Standards, Experimental Methods, and Protocols* **2013**, DOI: 10.1007/978-1-4614-8298-7.

DOI: 10.1021/acsnano.6b02083
ACS Nano 2016, 10, 5525−5535

(66) Sun, J.; Liu, C.; Yang, P. Surfactant-Free, Large-Scale, Solution–Liquid–Solid Growth of Gallium Phosphide Nanowires and Their Use for Visible-Light-Driven Hydrogen Production from Water Reduction. *J. Am. Chem. Soc.* **2011**, *133*, 19306–19309.
(67) Cardon, F.; Gomes, W. On the Determination of the Flat-Band Potential of a Semiconductor in Contact with a Metal or an Electrolyte from the Mott-Schottky Plot. *J. Phys. D: Appl. Phys.* **1978**, *11*, L63.
(68) Van Wezemael, A.-M.; Laflere, W.; Cardon, F.; Gomes, W. Study of the Schottky Barrier at the N-and P-Type Indium Phosphide Electrode/Electrolyte Interface. *J. Electroanal. Chem. Interfacial Electrochem.* **1978**, *87*, 105–109.
(69) Cooper, G.; Turner, J. A.; Parkinson, B. A.; Nozik, A. J. Hot Carrier Injection of Photogenerated Electrons at Indium Phosphide–Electrolyte Interfaces. *J. Appl. Phys.* **1983**, *54*, 6463–6473.
(70) Dominey, R. N.; Lewis, N. S.; Wrighton, M. S. Fermi Level Pinning of P-Type Semiconducting Indium Phosphide Contacting Liquid Electrolyte Solutions: Rationale for Efficient Photoelectrochemical Energy Conversion. *J. Am. Chem. Soc.* **1981**, *103*, 1261–1263.
(71) Dai, P.; Li, W.; Xie, J.; He, Y.; Thorne, J.; McMahon, G.; Zhan, J.; Wang, D. Forming Buried Junctions to Enhance the Photovoltage Generated by Cuprous Oxide in Aqueous Solutions. *Angew. Chem., Int. Ed.* **2014**, *53*, 13493–13497.
(72) Munoz, A.; Heine, C.; Lublow, M.; Klemm, H.; Szabo, N.; Hannappel, T.; Lewerenz, H.-J. Photoelectrochemical Conditioning of Movpe P-InP Films for Light-Induced Hydrogen Evolution: Chemical, Electronic and Optical Properties. *ECS J. Solid State Sci. Technol.* **2013**, *2*, Q51–Q58.
(73) Shaner, M. R.; Fountaine, K. T.; Lewerenz, H.-J. Current-Voltage Characteristics of Coupled Photodiode-Electrocatalyst Devices. *Appl. Phys. Lett.* **2013**, *103*, 143905.
(74) Kim, T. W.; Choi, K.-S. Nanoporous Bivo4 Photoanodes with Dual-Layer Oxygen Evolution Catalysts for Solar Water Splitting. *Science* **2014**, *343*, 990–994.
(75) Kanan, M. W.; Nocera, D. G. *In Situ* Formation of an Oxygen-Evolving Catalyst in Neutral Water Containing Phosphate and Co2+. *Science* **2008**, *321*, 1072–1075.
(76) Resasco, J.; Zhang, H.; Kornienko, N.; Becknell, N.; Lee, H.; Guo, J.; Briseno, A. L.; Yang, P. $TiO_2/BiVO_4$ Nanowire Heterostructure Photoanodes Based on Type II Band Alignment. *ACS Cent. Sci.* **2016**, *2*, 80.
(77) Kuang, Y.; Jia, Q.; Nishiyama, H.; Yamada, T.; Kudo, A.; Domen, K. A. Front-Illuminated Nanostructured Transparent $BiVO_4$ Photoanode for >2% Efficient Water Splitting. *Adv. Energy Mater.* **2016**, *6*, 10.1002/aenm.201501645.

DOI: 10.1021/acsnano.6b02083
ACS Nano 2016, 10, 5525–5535